ROYAL SOCIETY
OF CHEMISTRY

PAPER

Check for updates

Substitutional Mo doping in a Ta₃N₅ photoanode: mitigating native defects through engineering and enhancing water-splitting performance †

Hameed Ullah,*[a,b] Altaf Ur Rahman,[a,c] Ariadne Koche, [iD][b] Carlos F. O. Graeff, [iD][b] Marcus V. Castegnaro,[a] Marcos Jose leite Santos [iD][d] and Sherdil Khan [iD]*[a]

Ta₃N₅, with its 2.1 eV bandgap and favorable band edge positions, is a promising compound for solar water splitting. However, its performance is limited by defective states introduced during high-temperature nitridation, particularly those based on reduced Ta species that act as electron recombination centers and can pin the Fermi level. Increasing electron density to extend the conduction band may suppress the formation of these states. Here, we introduce a combined theoretical and experimental study on Mo doping in Ta₃N₅, aiming to inhibit structural defects and enhance photoelectrochemical activity. Theoretical calculations reveal that Mo doping in Ta₃N₅ not only decreases the bandgap but also transforms the material from an indirect to a direct bandgap semiconductor. This transformation is attributed to the ability of Mo^{4+} ions, with comparable ionic radii and oxidation states for substitutional doping. This substitution introduces neutralizing acceptor states, effectively mitigating the formation of reduced Ta^{3+}/Ta^{4+} states and nitrogen vacancies. As a result, charge carrier transport is enhanced, and recombination is suppressed. Additionally, the refractive index increases from 2.65 to 2.89 upon Mo doping, demonstrating improved optical performance for photoelectrochemical applications. Experimental results demonstrate a 4.3-fold enhancement in photoelectrochemical activity, alongside a 150 mV cathodic shift in the onset potential with substitutional Mo doping in Ta₃N₅. Moreover, the substitutional Mo doping does not induce lattice strain. These findings suggest that precise Mo doping in Ta₃N₅ has the potential to drive the development of innovative photoelectrochemical systems for practical solar fuel applications.

1. Introduction

To address global energy and environmental challenges, converting solar energy into chemical fuels offers a sustainable solution. Photoelectrochemical (PEC) water splitting represents a cutting-edge approach to producing green hydrogen by harnessing sunlight.[1] Metal oxides have been extensively studied as photocatalytic materials for artificial photosynthesis. However, their wide bandgaps and short charge diffusion lengths hinder their viability for large-scale, commercial applications. For example, TiO_2 [2–5] and WO_3 only absorb

UV light, representing 5% of the solar spectrum. Furthermore, due to very low charge carrier mobilities, other materials, such as $BiVO_4$,[6,7] Cu_2O,[8] CdS,[9] Fe_2O_3,[10] and $BaTaON$,[11] exhibit low water-splitting performances, which limit their practical applications. Efforts have been made to improve the optical and electronic properties of these materials. Metal nitrides have also been explored as photocatalysts. Among the various metal nitrides, Ta₃N₅ stands out due to its low bandgap ($E_g \approx 2.1$ eV) and favorable band edge positions that straddle the water redox potentials. Theoretically, Ta₃N₅ can achieve a photocurrent density of 12.9 mA cm⁻² and a maximum solar-to-hydrogen (STH) conversion efficiency of 15.9% under AM 1.5G illumination.[12] However, its overall water-splitting efficiency is significantly limited by charge carrier transport behavior, particularly the hole diffusion length and trapping of the electrons by interband states. The disparity between the short hole diffusion length (typically 5–50 nm) and the much larger light absorption depth at the micrometer scale poses a critical challenge, leading to increased charge recombination and reduced PEC performance. Similarly, the most common point defects associated with Ta₃N₅ are nitrogen vacancies (V_N) and reduced tantalum species

[a]Laboratory of Nanomaterials for Renewable Energy and Artificial Photosynthesis. Universidade Federal Do Rio Grande Do Sul, Porto Alegre, Brazil. E-mail: Sherdil.khan@ufrgs.br, hameedktk331@gmail.com

[b]Department of Physics and Meteorology, School of Sciences, Sao Paulo State University (UNESP), Bauru, Sao Paulo, 17033-360, Brazil

[c]Department of Physics, Riphah International University, Chamru Pur Lahore, Punjab 54000, Pakistan

[d]Institute of Chemistry – UFRGS, 91501-970 Porto Alegre, RS, Brazil

†Electronic supplementary information (ESI) available. See DOI: https://doi.org/10.1039/d4nr05198j

(*e.g.* Ta^{3+}). These point defects, *i.e.* V_N and Ta^{3+}, correspond to the formation of states that lie near the conduction band and play a vital role in destabilizing the material.[13] They also act as photogenerated charge carrier trap and recombination centers, affecting the PEC characteristics of Ta_3N_5.[14] To improve the PEC performance of Ta_3N_5, it is crucial to develop strategies that suppress or passivate these defects.

Various strategies have been investigated to overcome the challenges related to trapping and the transport of charge carriers in Ta_3N_5, including exploring nanostructure formation,[15] implementing heterojunctions,[16,17] and optimizing synthesis conditions.[18,19] Furthermore, the doping of different foreign ions into the lattice of Ta_3N_5 has been explored, resulting in enhanced PEC performance. To date, a broad spectrum of dopant ions in Ta_3N_5 has been investigated in the literature including Ba^{2+},[17] Mg^{2+},[20] W^{5+},[21] Zr^{4+},[22] Ge^{4+} (ref. 23) and Na^{1+}.[24] These dopants contribute to enhancements in the photoelectrochemical (PEC) characteristics of Ta_3N_5. These investigations indicated that the primary function of these dopants is to mitigate the presence of native point defects (V_N and Ta^{3+}) and facilitate the introduction of lattice oxygen. A notable example is substitutional Zr^{4+} doping in Ta_3N_5, where Zr^{4+} acts as a compensating electron acceptor. This doping effectively reduces the concentration of native defect states, such as nitrogen vacancies (V_N) and reduced tantalum states (Ta^{3+}), thereby improving the material's electronic properties.[11,25] Enhancing the Zr concentration results in an elevation of lattice oxygen, accompanied by the generation of defect pairs possessing lower formation energy when compared to isolated Ta_3N_5.[22,26] Li *et al.* achieved a 26.4% improvement in photocurrent density at 1.23 V_{RHE} through the incorporation of Ba into Ta_3N_5. Xiao *et al.* synthesized nanoparticles of Mg–Zr co-doped Ta_3N_5, which exhibit more favorable bandgap energetics, reducing the onset potential to 0.55 V_{RHE}. Consequently, the photocurrent density increases significantly to 2.3 mA cm^{-2} at 1.23 V_{RHE}.[25] Recently, Wagner and colleagues fabricated Ti-doped Ta_3N_5, demonstrating improved charge transport and enhanced photoconversion efficiency.[26] Mo is a transition metal with unoccupied d-states and an ionic radius of Mo^{4+} (~65 pm), which is comparable to that of Ta^{5+} (~64 pm). This similarity suggests that substitutional doping of Mo at the Ta site can occur without significantly altering the crystal structure of Ta_3N_5. Additionally, Mo has a lower oxygen affinity than Zr, which has been previously investigated as a dopant. As a result, during the nitridation process, Mo–O bonds can be more easily replaced by Mo–N bonds. Furthermore, the d-orbitals of Mo^{4+} can hybridize with Ta-d and N-p states, leading to an increase in electron density in the conduction band, thereby enhancing electron mobility. Despite these promising attributes, no prior theoretical or experimental studies have been reported on Mo doping in Ta_3N_5, leaving a critical gap in the understanding and optimization of this material for advanced applications.[27]

Aiming to inhibit structural defects and improve PEC performance of Ta_3N_5, herein, we conducted a comprehensive theoretical investigation of the impact of Mo doping in Ta_3N_5 and experimentally prepared Mo-doped Ta_3N_5 nanotubular photoelectrodes for photoelectrochemical (PEC) water splitting. To the best of our knowledge this is the first experimental and theoretical study of Mo-doped Ta_3N_5. This study aims to enhance the PEC performance of Ta_3N_5 photoanodes through Mo doping and to investigate their structural, electronic and optical properties using theoretical and experimental approaches. This work demonstrates that Mo doping effectively reduces deep-level defects and recombination centers associated with nitrogen vacancies and reduced tantalum states, leading to improved PEC activity, including a cathodic shift in the onset potential and enhanced photocurrent density. This study provides a comprehensive insight into the role of Mo in optimizing Ta_3N_5 for practical solar water-splitting applications.

2. Computational study

2.1 Computational method and model

The ground state, structural and electronic properties of bare and Mo-doped Ta_3N_5 were calculated by density functional theory (DFT). The DFT calculations in this study were performed by using the QUANTUM ESPRESSO (QE) package,[28] with the plane wave basis pseudopotential method. We used the generalized gradient approximation (GGA)[29] and GGA+U[30] in this study for the exchange correlation functionals. The charge density and wave-function cutoff used in the calculations are 280 Ry and 70 Ry, respectively. The residual force criterion used in the geometry relaxation is below 0.001 eV Å^{-1}. The valence electronic configurations used in this calculation are $2s^2 2p^3$ for N, $4d^5 5s^1$ for Mo and $5d^3 6s^2$ for Ta. Ultrasoft pseudopotentials are used for calculating the structural and electronic properties, whereas the norm-conserving pseudopotentials developed by the Fritz Haber Institute (FHI) are employed for optical property calculations.[31]

Note that the GGA functional is generally more reliable to calculate the thermodynamics and elastic properties.[32] However, the GGA functional tends to underestimate the bandgap energy, making it potentially insufficient for accurately calculating the electronic bandgap energy of semiconductors, especially in cases involving elemental doping.[33] To make the theoretical calculations more reliable and closer to the experimental results as much as possible we employed a GGA+U method in this study. In the GGA+U method, an on-site Coulomb interaction is added to the selected orbitals. Due to the Coulomb energy added to the selected orbitals an upshift is observed in the conduction band (CB), while the occupied state energy remains the same. The GGA+U method is applied to correctly describe the bandgap structure of bare and Mo-doped Ta_3N_5. Details of the Hubbard parameter are provided in the ESI.†[34–38] The accuracy of the GGA+U method is determined by parameter *u*. In our calculation, *u* values are set at 0.1 and 0.2. Using the *u* value 0.2, the calculated bandgap of bare Ta_3N_5 (2 eV) is in good agreement with experimental bandgap (2.1 eV) results.

2.2 Formation energy calculation method

The formation energy (E_f) is defined as:

$$E_f = E_{Defect} - E_{Pure} + \mu_{host} - \mu_x \tag{1}$$

where E_{Defect} and E_{Pure} are the total energies of the Ta_3N_5 unit cell with and without defects, respectively. μ_{host} and μ_x are the chemical potentials of the substituted species and dopant atom, respectively. Eqn (1) indicates that a more negative formation energy results in more favorable elemental doping.[32]

2.3 Theoretical results and discussion

2.3.1 Structural properties. The compound Ta_3N_5 possesses an orthorhombic crystal structure characterized by the space group *CmCm*. Its conventional unit cell contains 32 atoms, in total. In this structure, each tantalum (Ta) atom is coordinated with six nitrogen (N) atoms, while each nitrogen atom interacts with three to four tantalum atoms (see Fig. 1). Initially, both the bare and molybdenum (Mo) doped Ta_3N_5 were optimized using the generalized gradient approximation (GGA) and GGA+U functionals. In the bare Ta_3N_5, the calculated Ta–N bond lengths along the three crystallographic axes (x, y, and z) are measured at 2.95 Å, 1.97 Å, and 2.04 Å, respectively. Following Mo doping at the Ta site with the highest x coordinate, the corresponding Ta (Mo)–N bond lengths along the x, y, and z directions were reduced to 2.03 Å, 1.86 Å, and 2.01 Å, respectively. These variations in bond lengths can be attributed to the difference in electronegativity between Ta (1.5) and Mo (2.16). Comparative analyses of the lattice constants for both bare and Mo-doped Ta_3N_5 are depicted in Fig. S1 and S2,† revealing minimal changes post-Mo doping, as summarized in Table 1.[39] The slight variation can be explained by the similar ionic radii of Ta (64 Å) and Mo (65 Å). Notably, the GGA+U functional did not significantly alter the bond lengths or lattice constants, as the u parameter value was maintained at a relatively low level (refer to Table S2†).
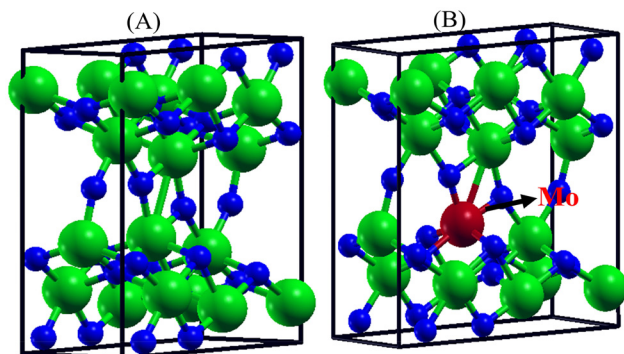

Fig. 1 The crystal structure of (A) Ta_3N_5 and (B) Mo-doped Ta_3N_5. The semiconductor has an orthorhombic crystal structure with space group CmCm. The Mo, N and Ta atoms are shown as red, blue and green spheres, respectively.

Table 1 Calculated lattice parameters of bare and Mo-doped Ta_3N_5, obtained by using GGA and GGA+U functionals

Lattice parameters	This work (bare Ta_3N_5)		This work (Mo-doped Ta_3N_5)		Previous work (bare Ta_3N_5)	Ref.
	GGA	GGA+U	GGA	GGA+U		
a (Å)	3.88	3.88	3.89	3.89	3.89	39
b (Å)	10.26	10.27	10.27	10.28	10.26	31
c (Å)	10.30	10.31	10.31	10.31	10.31	40 and 31
α (°)	90.0	90.0	90.0	90.0	90.0	41
β (°)	90.0	90.0	90.0	90.0	90.0	42
γ (°)	90.0	90.0	90.0	90.0	90.0	42 and 31

2.3.2 Electronic structures. We conducted GGA and GGA+U calculations using optimized geometries. As shown in Fig. 2 (A), bare Ta_3N_5 is an indirect bandgap semiconductor. The valence band maximum (VBM) is between the Z and R points of the Brillouin zone, and the conduction band minimum is at the R point of the Brillouin zone. Fig. 2(A) also displays projected densities of states (PDOS) of bare Ta_3N_5 indicating that the conduction band (CB) is primarily composed of Ta 5d orbitals, while N 2p orbitals dominate the valence band (VB). For bare Ta_3N_5, the calculated bandgap with GGA is 1.32 eV. These results show good agreement with previous literature.[43,44] Due to the unoccupied d-orbitals of Ta and Mo, partial substitution of Ta by Mo in Ta_3N_5 causes the hybridization of Ta 5d and Mo 4d, which results in more delocalized orbitals in the CB which can be clearly seen in the PDOS in Fig. 2(B). These delocalized orbitals in the CB may contribute to enhanced light absorption. Substitutional doping of Mo in Ta_3N_5 not only reduced the bandgap energy but also changed the nature of the bandgap from indirect to direct. In band structure calculations, a material is classified as a direct bandgap semiconductor if the conduction band minimum (CBM) and valence band maximum (VBM) are located at the same wave vector (k-point). Conversely, if they appear at different wave vectors, the material is considered an indirect bandgap semiconductor. In the present case, Mo doping in Ta_3N_5 induces a transformation in the band structure, shifting the material from an indirect to a direct bandgap semiconductor. The calculated bandgap for Mo-doped Ta_3N_5 with GGA is 0.94 eV at the Γ point (Fig. 2(B)). The DFT study reveals that Mo doping created some extra energy states near the conduction band, which may enhance the n-type conductivity of the CB and lead to enhanced light absorption.

The band structure and partial density of states (PDOS) for both bare and Mo-doped Ta_3N_5, calculated using the GGA+U method, are illustrated in Fig. 2(C) and (D). The results indicate that bare Ta_3N_5 behaves as an indirect bandgap semiconductor, with the conduction band minimum (CBM) and valence band maximum (VBM) positioned at the R and Γ points of the Brillouin zone. This finding is consistent with previous experimental and theoretical studies, confirming the indirect bandgap nature of bare Ta_3N_5.[19,44] Meanwhile, Mo-doped Ta_3N_5 exhibits direct band conduction. The introduc-
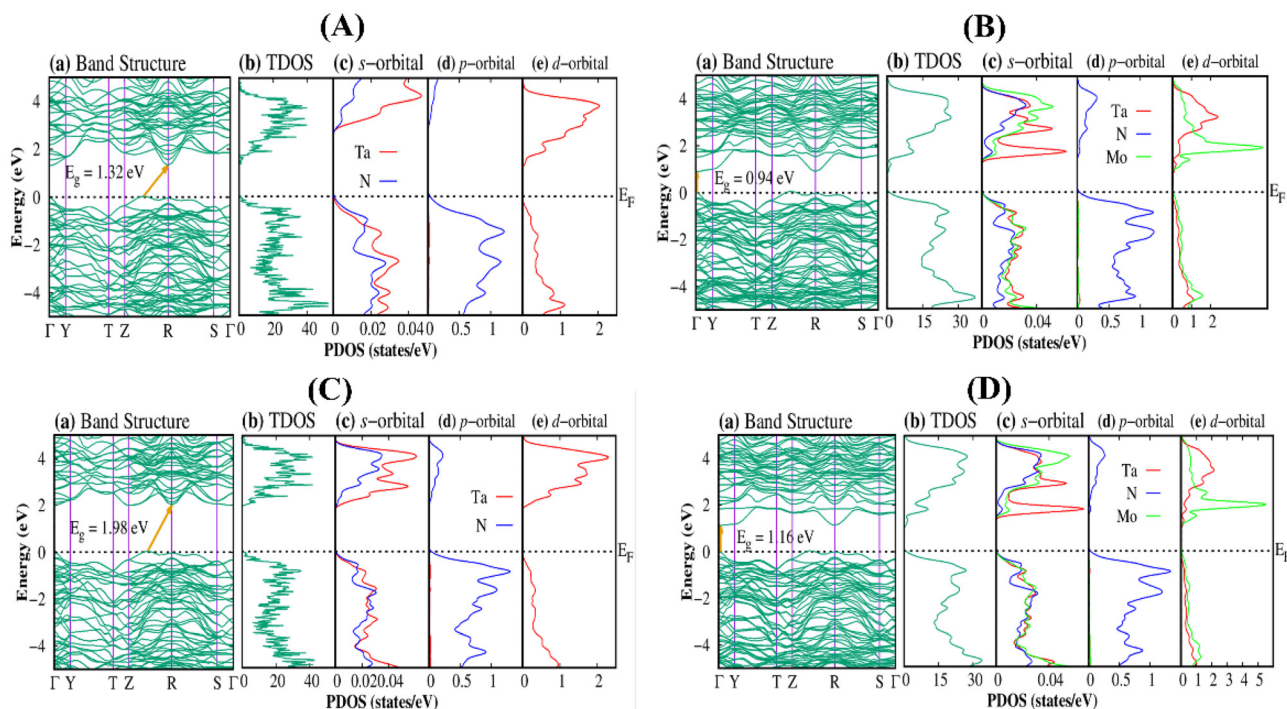
Fig. 2 GGA-calculated bandgap and projected density of states (PDOS) for (A) bare Ta_3N_5 and (B) Mo-doped Ta_3N_5. GGA+U-calculated bandgap and PDOS for (C) bare Ta_3N_5 and (D) Mo-doped Ta_3N_5.

tion of the Hubbard U parameter alters the potential profile of the unit cell, resulting in an increased bandgap energy compared to the GGA calculations. Specifically, the calculated indirect bandgap energies are 1.87 eV for $u = 0.1$ (Fig. S3†) and 1.98 eV for $u = 0.2$ (Fig. 2(C)). This increase is attributed to the Coulomb interaction, which localizes electrons in the d and f orbitals. As these localized states, which are situated near the Fermi energy in the bandgap, are pushed further away by the introduction of the Hubbard U parameter, the bandgap energy subsequently rises.[45] In contrast, Mo doping results in a reduced bandgap energy of 1.16 eV, as depicted in Fig. 2(D). The presence of additional energy states from the Mo 4d orbitals (Fig. 2(D)(d)) near the conduction band mitigates charge recombination by decreasing deep traps often associated with nitrogen vacancies (V_N) and reduced Ta^{3+} species. By trapping the CB electrons, Wang et al. theoretically demonstrated that they could convert O_N^* single positive charge states and O_N^{***} triple positive charge states in Ta_3N_5 into $O_N^×$ neutral charge states and O_N^* single positive charge states.[46,47] Therefore, Mo doping will make it possible for the charge carrier to move to the semiconductor's surface instead of going to the trapping states, where it may result in enhanced charge carrier mobility and PEC water-splitting performances. The theoretically calculated bandgap and formation energy are shown in Table 2.

2.3.3 Optical properties. The methodology for extracting optical properties from the dielectric function is well-documented in the literature.[48] Regarding the electronic properties, the calculated bandgap energy for pristine and Mo-doped Ta_3N_5 using $u = 0.2$ is in close agreement with experimental values.

**Table 2** The calculated bandgap and lattice constants of bare and Mo-doped Ta

u	Sample	Band gap	E_{form} (eV per unit cell)
0.1	Ta_3N_5	1.87	−9.90
0.1	$Mo-Ta_3N_5$	1.06	−8.96
0.2	Ta_3N_5	1.98	−9.30
0.2	$Mo-Ta_3N_5$	1.16	−8.86

Accordingly, all optical properties were computed using the GGA+U approach with $u = 0.2$. Fig. 3(a) and (b) depict the calculated imaginary part of the dielectric function $\varepsilon_2(\omega)$ for bare and Mo-doped Ta_3N_5 as a function of photon energy. $\varepsilon_2(\omega)$ exhibits a sharp increase at the bandgap energy, followed by a peak as the photon energy rises. Using GGA, the maximum $\varepsilon_2(\omega)$ values were observed at approximately 2.0 eV for bare Ta_3N_5 and 1.0 eV for Mo-doped Ta_3N_5. After applying the U correction, these transitions shifted to 2.50 eV and 1.47 eV, respectively. These transitions correspond to electronic excitations from N 2p states to Ta 5d states in bare Ta_3N_5, and from N 2p to Ta 5d + Mo 4d states in Mo-doped Ta_3N_5. Our findings align well with previous studies by A. H. Reshak et al.,[49] who reported peaks in $\varepsilon_2(\omega)$ near 2.9 eV and 2.6 eV. A comparison of the threshold energies with the electronic bandgap values (Table S4†) reveals excellent agreement between the electronic and optical bandgaps for both bare and Mo-doped Ta_3N_5.

The peak positions in $\varepsilon_2(\omega)$ are indicated in Fig. 3(b), with bare Ta_3N_5 at 2.50 eV (red dotted line) and Mo-doped Ta_3N_5 at
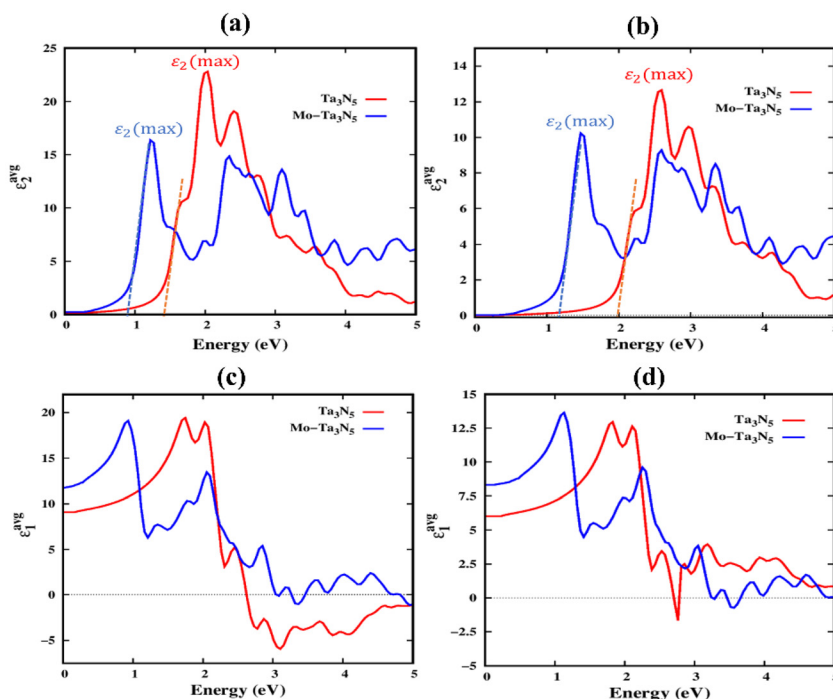
Fig. 3 (a) The imaginary part of the dielectric function for bare and Mo-doped Ta_3N_5, calculated using GGA. (b) The imaginary part of the dielectric function for bare and Mo-doped Ta_3N_5, obtained from GGA+U calculations. (c) The real part of the dielectric function for bare and Mo-doped Ta_3N_5, computed using GGA. (d) The real part of the dielectric function for bare and Mo-doped Ta_3N_5, calculated with GGA+U (u = 0.2).

1.47 eV (blue dotted line) under the GGA+U framework. This downward shift in energy for Mo-doped Ta_3N_5 signifies enhanced photon absorption in the visible spectrum due to doping. Additionally, the imaginary part of the dielectric function closely corresponds to the absorption coefficient, as shown in Fig. S4.† Mo doping increases the absorption spectrum by approximately 30% in the low-energy range, slightly outperforming bare Ta_3N_5. This enhancement is consistent with the trend observed in the spectra of $\varepsilon_2(\omega)$ (Fig. 3(a) and (b)).

Fig. 3(c) and (d) present the real part of the dielectric function ($\varepsilon_1(\omega)$) for bare and Mo-doped Ta_3N_5 as a function of photon energy, calculated using both GGA and GGA+U functionals. The real part of the dielectric function provides insight into the material's polarization response under electromagnetic radiation. By analyzing $\varepsilon_1(\omega)$, the static dielectric constant, corresponding to zero frequency ($\omega \to 0$), can be determined. The calculated static dielectric constants are summarized in Table S4.† For bare Ta_3N_5, the static dielectric constant derived using GGA+U aligns well with values reported in previous literature.[49] For Mo-doped Ta_3N_5, no prior studies are available for direct comparison. Furthermore, the polarization peaks observed in Fig. 3 reveal pronounced anisotropy in the dielectric response of both bare and Mo-doped Ta_3N_5. This anisotropy underscores the complex interactions between the electronic structure and electromagnetic fields, particularly in the doped system.

The zero-frequency reflectivity of bare and Mo-doped Ta_3N_5, calculated using the GGA approximation, are 27% and 21%,

respectively, as shown in Fig. 4(a). For bare Ta_3N_5, the maximum reflectivity reaches 60% at 4 eV, whereas for Mo-doped Ta_3N_5, it is 37% at 1.02 eV. These values are higher than those reported in previous literature, which is likely due to the GGA approximation, which tends to overestimate optical properties. When using the GGA+U method, the calculated zero-frequency reflectivity values for bare and Mo-doped Ta_3N_5 decrease to 21% and 16%, respectively (Fig. 4(b)). Additionally, the reflectivity at the optical bandgap was calculated for both bare and Mo-doped Ta_3N_5. For bare Ta_3N_5, the reflectivity is 35%, in excellent agreement with previously reported values.[49] In contrast, Mo doping reduces the reflectivity to 29% at the optical bandgap. This reduction in reflectivity upon Mo doping suggests enhanced light absorption in the visible region, which can be linked to the modified electronic structure.

Fig. 4(c) and (d) show the refractive indices of bare and Mo-doped Ta_3N_5 as a function of photon energy, calculated using GGA and GGA+U methods. The higher electron density increases the probability of photon–electron interaction. The GGA-calculated static refractive index $\eta(0)$ for bare Ta_3N_5 is 3.41, slightly higher than the previously reported value of 3.23. For Mo-doped Ta_3N_5, the GGA-calculated static refractive index is 3.75, with no prior literature available for comparison. This increase in the static refractive index value is attributed to the donor behavior of Mo. The GGA+U-calculated static refractive indices for bare and Mo-doped Ta_3N_5 are 2.51 and 2.89 (Fig. 4(d)), respectively. The reported value for bare Ta_3N_5
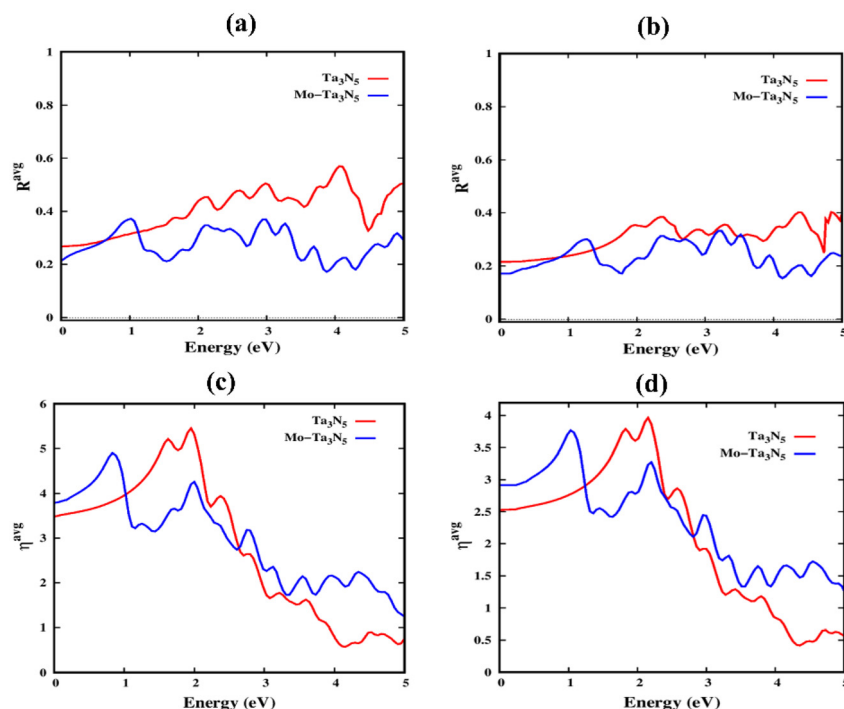
Fig. 4 Reflectivity of bare and Mo-doped Ta_3N_5 calculated using (a) GGA and (b) GGA+U. Refractive index of bare and Mo-doped Ta_3N_5 computed using (c) GGA and (d) GGA+U with u = 0.2 eV.

using GGA+U is 2.65. The refractive index follows a typical trend: it increases with photon energy, peaks, and then declines, consistent with the optical properties discussed earlier. The findings presented by the DFT calculations indicate that Mo is an excellent dopant for tailoring the absorption properties and bandgap characteristics of Ta_3N_5.

3. Experimental

3.1 Mo-doped Ta_3N_5 nanotube preparation

Tantalum foils (10 mm × 10 mm × 0.25 mm, Alfa Aesar, purity 99.95%) were prepared by mechanical polishing with sandpaper ranging from 400 to 1200 grit to achieve a mirror-like finish. The foils were then cleaned by sequential ultrasonication in acetone, ethanol, isopropanol, and deionized water, each for 30 min, and dried with nitrogen before anodization.

Anodization was conducted in a two-electrode setup with the Ta foil as the anode and a copper disc as the cathode, spaced 1 cm apart. The electrolyte consisted of H_2SO_4, 1% HF, and 4% H_2O. A constant voltage of 50 V was applied for 20 min at 10 °C. After anodization, the samples were rinsed with deionized water and dried with nitrogen.

To prepare Mo-doped Ta_2O_5, sodium molybdate (Na_2MoO_4) solutions of 0.1, 0.3, and 0.5 M were prepared, with Ta_2O_5 foils placed in an autoclave with the solution and heated to 180 °C for 12 h. The samples were then dried at 80 °C for 6 h. Mo-doped Ta_3N_5 nanotubes (NTs) were synthesized through

ammonolysis at 900 °C for 3 h with a 125 sccm ammonia flow in a horizontal quartz tube furnace, with heating and cooling rates of 10 °C min^{-1}.[22] Samples were then cooled under constant ammonia flow, washed with deionized water, and dried.

For photoelectrochemical (PEC) testing, both bare and Mo-doped Ta_3N_5 samples (denoted MTN-X, where X = 0.1, 0.3, and 0.5 M) had their rear surfaces polished to expose the conductive Ta substrate to copper wire. Copper wire was attached to this surface with silver epoxy, and the samples were sealed with non-conductive epoxy, leaving the test area exposed.

3.2 Co-catalyst modification

The surfaces of both bare and Mo-doped Ta_3N_5 were enhanced through co-catalyst modification to improve hole transfer in photoelectrochemical (PEC) applications. $Co(OH)_x$ was used as an oxygen evolution co-catalyst. To prepare this co-catalyst, a solution containing 0.1 M $Co(NO_3)_2$ and 0.1 M NaOH was stirred for 1 h to ensure homogeneity. Next, the bare and Mo-doped Ta_3N_5 samples were immersed in the prepared solution for 1 h, then thoroughly rinsed with deionized water and air-dried. After modification, the samples were designated as follows: Ta_3N_5 with co-catalyst as Ta_3N_5-Co, and Mo-doped Ta_3N_5 with co-catalyst as MTN-X-Co, where X represents the Mo concentration (0.1, 0.3, or 0.5 M). These samples were then subjected to PEC testing.

3.3 Structural characterization

The crystal structures of all bare and Mo-doped Ta_3N_5 NTs were investigated with a Bruker D8 Advance X-ray diffract-

ometer with Cu Kα radiation (λ = 1.54 Å) at 40 kV and 40 mA. Grazing incidence X-ray diffraction was carried out at a fixed incident angle of ω = 0.2°, with a 2θ range from 5° to 75° and a 0.01° step size, and the measuring time per step was 2 s. The surface morphology and elemental distribution were examined using a Zeiss EVO 50 scanning electron microscope (SEM) equipped with energy dispersive X-ray spectroscopy (EDX) equipment, operating at 10 kV. To investigate the chemical fingerprint of bare and Mo-doped Ta$_3$N$_5$, Raman spectroscopy was performed by using a HORIBA confocal Raman microscope. The nanotubular morphology was examined using a JEOL JEM-1400 flash transmission electron microscope (TEM), operating at 120 kV. The samples were dispersed in isopropyl alcohol and sonicated for 10 min. The solution was then dropped onto a copper grid covered with a holey carbon membrane for TEM observation. X-ray photoelectron spectroscopy (XPS) was performed to analyze the surface chemical states of all samples by using an Omicron-SPHERA station with an Al-Kα X-ray source. The XPS data was analysed using the CasaXPS software. The C 1s peak associated with adventitious carbon was anchored at 284.6 eV to establish and calibrate the binding energy scale. The measurements of the samples were conducted without adhering to a specific systematic order; all samples were measured consecutively. Additionally, there was no evidence of sample charging observed during the measurement process. The UV-Vis diffuse reflectance spectra of Ta$_3$N$_5$ samples were recorded by using the CARY 5000 spectrophotometer. The bandgaps of all Ta$_3$N$_5$ samples were calculated by converting the spectra Tauc plots by using the following equation:

$$\alpha h\nu = A(h\nu - E_g)^{\frac{1}{2}} \tag{2}$$

where α is the absorption coefficient, h is the Planck constant, ν is the incident light frequency, A is a constant and E_g is the energy of the bandgap. According to the above eqn (2), the bandgap of the material, either bare or doped Ta$_3$N$_5$, can be calculated easily by drawing a tangent line to the light absorption position and to the high absorption background through fitting $(\alpha h\nu)^2$ *vs.* $h\nu$.

3.4 Photoelectrochemical measurement characterization

PEC measurements were conducted utilizing the Gamry Interface 1000 potentiostat, which incorporates a three-electrode configuration cell. The testing electrolyte employed for these measurements was a 1 mol L^{-1} KOH solution. In the PEC cell the Ta$_3$N$_5$ photoanode was used as a working electrode, Ag/AgCl as a reference electrode, and Pt foil as a counter electrode. The measured potentials *versus* a Ag/AgCl reference electrode were converted to the reversible hydrogen electrode (RHE) scale by using the following equation:[50]

$$V_{RHE} = V^0_{Ag/AgCl} + V_{Ag/AgCl} + 0.0592 \times pH \tag{3}$$

Throughout the PEC experiment, a 300 W xenon lamp served as the light source for conducting photocurrent–voltage measurements on the working electrode. Before each PEC test,

the AM 1.5G filter was used to filter the polychromatic light and the light intensity was adjusted to 100 mW cm^{-2} (1 sun) by using a silicon diode. Before measuring the samples, the electrolyte was purged with Ar gas for 30 min. Linear sweep voltammetry (LSV) curves were obtained with a five-second manually chopped light-on and light-off cycle, employing a scan rate of 10 mV s^{-1}. Incident photon-to-current efficiency (IPCE) measurements were performed using a Keithley 2400 source measure unit, a xenon lamp (300 W) with an AM 1.5 filter and a Cornerstone Oriel monochromator, at 1.23 V *vs.* RHE. Electrochemical impedance spectroscopy (EIS) was performed over a frequency range of 10^5 to 0.1 Hz with a 10 mV amplitude at 1.23 V$_{RHE}$.

4. Results and discussion

4.1 Mo-doped Ta$_3$N$_5$ electrode characterization

Fig. 5(a) shows a schematic diagram of the synthesis procedure of pure and Mo-doped Ta$_3$N$_5$ on a Ta substrate. Ta was anodized to form Ta$_2$O$_5$ nanotubes and then Mo was incorporated hydrothermally prior to the nitridation process. Fig. S5(a and b)† shows the surface and cross-sectional scanning electron microscopy (SEM) images showcasing the as-anodized Ta$_2$O$_5$ nanotubes (NTs). Anodization facilitated the formation of robust Ta$_2$O$_5$ NTs, with growth controllable *via* adjustments in temperature and electrolyte composition.[51] The utilization of a relatively low electrolyte temperature led to strong adherence of the Ta$_2$O$_5$ NTs to the substrate. Moreover, to ensure mechanical stability, a low HF concentration, *i.e.* 1 vol%, was maintained. The average length and external diameter of the NTs measured were 2.1 μm and 160 nm, respectively. These findings align well with previous literature reports.[51]

To elucidate the influence of Mo on the morphology of the Ta$_3$N$_5$ nanotubes, we acquired top-view SEM images of the prepared samples and compared them with findings from the previous literature. In Fig. S5(c),† it is evident that the bare Ta$_3$N$_5$ nanotubes (NTs) exhibit an irregular surface, closely resembling the surface of Ta$_2$O$_5$ NTs. This observation suggests that the high-temperature nitridation process does not alter the morphology of the nanotubes, consistent with findings from previous literature.[52] The Mo-doped Ta$_3$N$_5$ nanotubes (NTs) are presented in Fig. S5(d–f)† for comparison. The SEM images of Ta$_3$N$_5$ reveal a polycrystalline surface with irregularly oriented agglomerates. The surface exhibits moderate porosity, likely improving light absorption and providing active sites for photocatalytic reactions. Clear grain boundaries are visible, which might influence the charge carriers.

Fig. 5(b–e) illustrate the cross-section SEM images of bare and Mo-doped Ta$_3$N$_5$ NTs prepared by nitration of Ta$_2$O$_5$ and Mo-Ta$_2$O$_5$ at 900 °C for 3 h. After nitration, a shrinkage in the NTs was observed as the measured average length of the NTs was decreased to ~1.5 μm. This shrinkage in the NTs is because of the replacement of N in place of O to maintain the charge conservation.[53] It can also be understood from the valence electron differences between O^{2-} and N^{3-} that
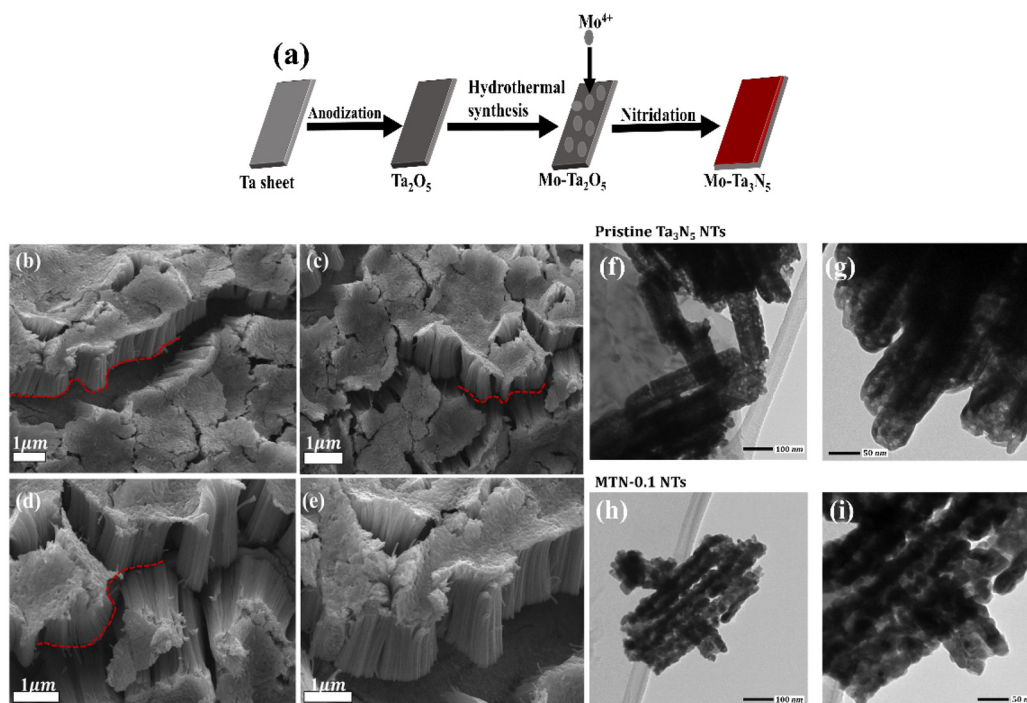
Fig. 5 (a) Schematic diagram of the synthesis process of Mo-doped Ta_3N_5 NTs (MTNs). Top-view SEM images of (b) Ta_3N_5, (c) MTN-0.1, (d) MTN-0.3 and (e) MTN-0.5. The red dashed line highlights the boundary between the Ta substrate and nitride layer. Transmission electron microscopy (TEM) images of (f), (g) Ta_3N_5, and (h), (i) MTN-0.1 NTs.

changed the coordination number. The decrease in the coordination number led to a change in the crystal structure and shrinkage of the NTs.[53] The measured average length of the nanotubes remained ~1.5 μm for Mo-doped Ta_3N_5, the same as that for bare Ta_3N_5. Fig. 5(f and g) show the TEM images of pure Ta_3N_5 NTs, while Fig. 5(h and i) show MTN-0.1 NTs. The images clearly confirm that both the pure and Mo-doped samples retain their NT-like structures.

To illustrate the homogeneous distribution of Ta, O, N, and Mo elements within the MTN-X NTs, plan view elemental mapping obtained through EDX is presented in Fig. S6† (0.1 M Mo). It is evident that with an increase in dopant (Mo) concentration, the weight percentage of Mo detected by EDX also increases, as demonstrated in Table S5.†

To investigate the crystal structure of the synthesized nanotubes, grazing incidence X-ray diffraction (GI-XRD) was performed, as shown in Fig. 6. The GI-XRD analysis reveals that nitridation of Ta_2O_5 at 900 °C induces a complete transformation of its crystal structure from orthorhombic Ta_2O_5 to orthorhombic Ta_3N_5.[54] Peaks at 2θ ~24.5°, 35°, and 36° correspond to the Miller indices [110], [130], and [113] for Ta_3N_5, respectively. Furthermore, with varying Mo content in Ta_3N_5, no additional peaks or peak shifts are observed indicating the successful synthesis of orthorhombic Ta_3N_5 NTs with a similar lattice constant and crystallinity. The preservation noted in the lattice parameters of the unit cell observed in this study can be attributed to the similarity in the ionic radii of Mo^{4+} and Ta^{5+}.[55] The structural compatibility arising from this similarity
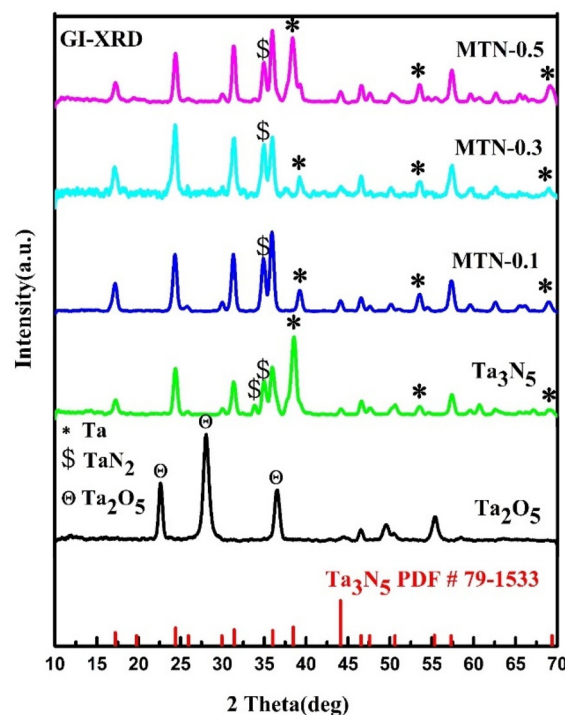
Fig. 6 GI-XRD patterns of bare Ta_3N_5 and Mo-doped Ta_3N_5. The standard is also included.

in ionic radii suggests the feasibility of structural doping with Mo_{Ta}. The experimental lattice constants obtained from XRD analyses are in good agreement with their theoretical values (Table S3†). Despite utilizing grazing angle XRD to minimize substrate contributions, signals from Ta_2N were observed at 2θ ~61°, attributed to its formation at the interface of the Ta substrate and the base of Ta_2O_5 nanotubes during nitridation.[56] This metallic phase has been identified as a significant electron transfer facilitator in existing literature.[26,50]

In Fig. 7(a), the absorption spectra of both bare Ta_3N_5 and MTN_x are depicted. The corresponding absorption edges (bandgaps) for all samples can be found in Table S6.† The absorption edges correspond to electronic transitions from nitrogen (N) 2p orbitals, which predominantly constitute the valence band, to tantalum (Ta) 5d orbitals that make up the conduction band. Although the observed changes in bandgap were not as pronounced, it is noteworthy that the Mo-doped samples exhibited a decrease in absorption tail at higher wavelengths above the bandgap. This decrease implies the suppression of reduced Ta species, a phenomenon frequently documented in the literature.[22,34] Additionally, the experimental transformation of Ta_2O_5 into Ta_3N_5 through nitridation does not entirely eliminate the presence of 3-coordinated lattice O, which significantly influences the crystal structure and optical properties of the synthesized Ta_3N_5.[56,57] The bandgap of all samples was calculated using the Tauc plot as given in Table S6.† X. Zou *et al.* reported Zr doping in Ta_3N_5, which displayed a similar trend in bandgap behaviour.[22]

The phase composition and microstructure of bare Ta_3N_5 and MTN_x were analyzed through Raman spectroscopy, as depicted in Fig. 8(a). The Raman spectra for all samples showcased a high degree of similarity, with no additional peaks detected, aligning well with the GI-XRD findings. The characteristic Raman spectra displayed frequencies at approximately $271\ cm^{-1} \pm 2\ cm^{-1}$, $405\ cm^{-1} \pm 2\ cm^{-1}$, $526\ cm^{-1} \pm 2\ cm^{-1}$, and $599\ cm^{-1} \pm 2\ cm^{-1}$, which are attributed to Ag vibration modes, while frequencies at around $496\ cm^{-1} \pm 2\ cm^{-1}$, $748\ cm^{-1} \pm 2\ cm^{-1}$, and $824\ cm^{-1} \pm 2\ cm^{-1}$ correspond to B_g vibration modes.[58] These observations are consistent with previously reported research on Ta_3N_5.[59] Notably, the Raman
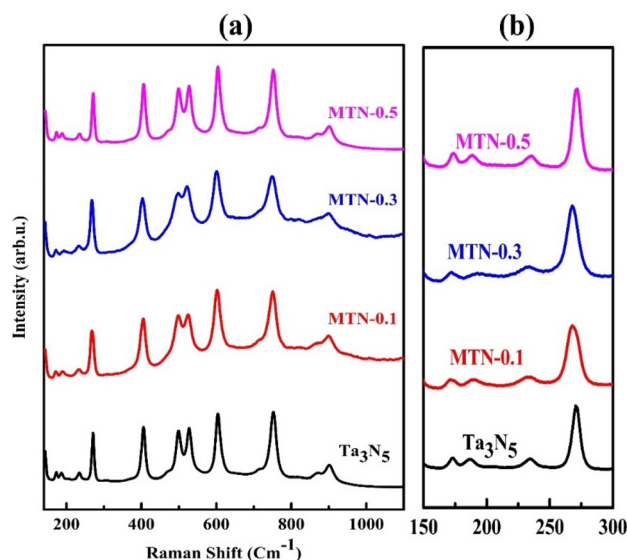

Fig. 8 (a) Raman scattering spectra of bare Ta_3N_5 and MTN_x samples; (b) the main A_g mode peak for bare Ta_3N_5 and MTN_x samples.

bands at $271\ cm^{-1} \pm 2\ cm^{-1}$ and $404.5\ cm^{-1} \pm 2\ cm^{-1}$ are associated with the bending vibrations of Ta–N–Ta, distinctly identifying the orthorhombic crystal structure of Ta_3N_5.[60] Intriguingly, Mo doping of Ta_3N_5 resulted in a noticeable shift in the A_g mode peak (Fig. 8(b)). Specifically, for the MTN-0.1 sample, the full width at half maximum (FWHM) of the Ag mode located at $271\ cm^{-1}$ is narrowed, with the peak position exhibiting a clear red shift, a trend similarly observed in the MTN-0.3 sample. However, as the Mo concentration continues to increase, the trend observed in the prominent Ag mode begins to reverse. This change suggests that at higher Mo levels, additional structural disorder is introduced into the Ta_3N_5 crystal lattice. These alterations imply that a high concentration of Mo disrupts the lattice stability, potentially affecting the material's overall properties.

The surface chemistry of bare and Mo-doped Ta_3N_5 was studied by XPS. The survey spectra (Fig. S10(a)†) collected for MTN_x, Ta_3N_5, and Ta_2O_5 (before nitridation) support the suc-
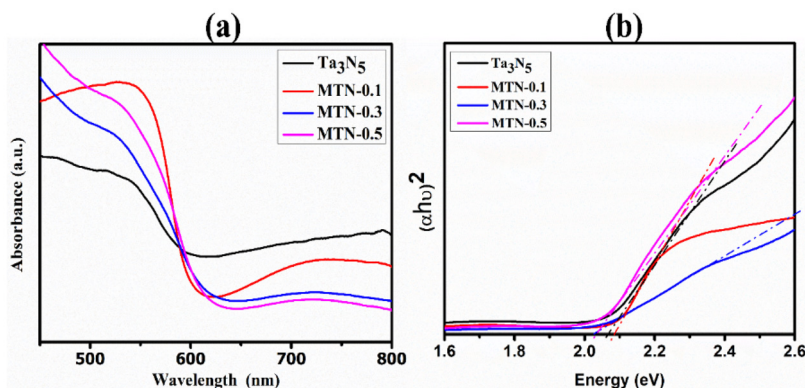

Fig. 7 UV-visible absorption spectra and (b) Tauc plots of bare Ta_3N_5 and MTN_x samples.

cessful nitridation, reflected by the increase of the N 1s peak and the decrease of the O 1s peak intensities. Despite the decrease in the O 1s intensity, the considerable amount of remaining O reinforces the incomplete removal of lattice O, a phenomenon frequently observed in previous literature.[57] The deconvolution of the O 1s peak (Fig. S10(B)†) indicated that some of the O surface species in bare and doped samples is in a TaO_xN_y chemical environment.[53,61] The Ta 4f doublet was deconvoluted (Fig. 9(A)), assuming two chemical environments for Ta species. These components are attributed to Ta_3N_5 (lower-energy doublet) and TaO_xN_x (higher energy doublet).[57,62,63] Ta $4f_{7/2}$ and Ta $4f_{5/2}$ peaks of MTN-0.1, MTN-0.3, and MTN-0.5 exhibit shifts and distinct spectral fea-

tures compared to bare Ta_3N_5. Upon doping with increasing amounts of Mo, progressive shifts toward higher BE were observed. These shifts reflect the changes in the local environment around Ta atoms (replacement of Ta by Mo) and in their electronic structure (enhanced electron density around Ta species). The differences between the electronic structures of Ta in bare and doped samples were evaluated by subtracting the Ta_3N_5 spectrum from the MTN-0.5 spectrum (Fig. 9(B)). The difference spectrum reveals two negative peaks at the lower BE regions (for pure Ta_3N_5) and two positive peaks at the higher BE regions (for pure Mo-doped Ta_3N_5). These results indicate that pure Ta_3N_5 exhibits reduced Ta species observed at lower binding energies (BE). Upon Mo doping, these low-BE
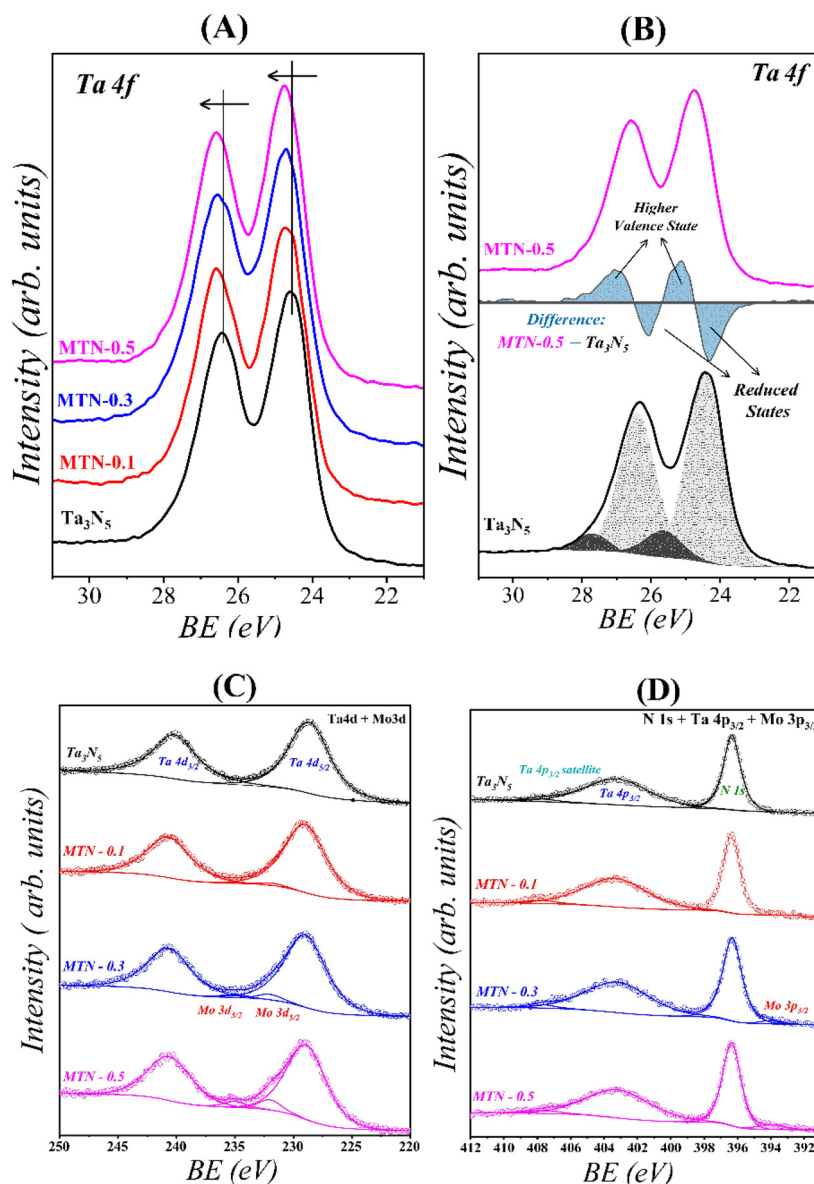
Fig. 9 XPS core level spectra of Ta and Mo: (A) representation of Ta 4f; (B) the spectrum difference between pure Ta_3N_5 and Mo-doped Ta_3N_5 with the residual higher and lower BE energy peaks. The difference was extracted by subtracting Ta_3N_5 data from MNT-0.5 data, after correction and normalization. Deconvoluted (C) Ta 4d and Mo 3d peaks and (D) N 1s, Ta 4p and Mo 3p PS spectra.

states are suppressed, evidenced by the positive BE peaks observed in the doped samples. This positive energy shift for Mo-doped Ta₃N₅ is attributed to the hybridization of Mo, Ta, and N valence orbitals, leading to an abundance of higher valence states. The introduction of donor levels by Mo doping reduces the prevalence of lower-energy states, thereby minimizing recombination centers and significantly improving charge carrier mobility. The introduction of Mo^{4+} stabilizes the electronic environment and balances the electronic structure by compensating for intrinsic defects, while creating favorable donor levels. These results agree with theoretical findings as shown in Fig. 2. The high-resolution spectra collected in the 250–220 eV range (Ta 4d and Mo 3d overlapped regions) and in the 412–392 eV range (Ta $4p_{3/2}$, Mo 3p and N 1s) confirmed the successful Mo incorporation into Ta₃N₅. However, the overlapping of Mo with Ta peaks (Fig. 9(C) and (D)) makes it difficult to extract reliable quantitative insights. The ratios of the peaks extracted from the deconvolution of the spectra are summarized in Table S7 (ESI†).

5. Water oxidation performance of bare Ta₃N₅ and MTN-X photoanodes with and without co-catalyst

Fig. 10(a) and (b) show the photoelectrochemical (PEC) performance of bare Ta₃N₅ and MTN-X samples, without and with $Co(OH)_x$ co-catalyst modification, respectively, as measured by linear sweep voltammetry (LSV). All LSV tests were conducted in a 1 M KOH electrolyte (pH 13.6) within a three-electrode PEC cell, under chopped AM 1.5G simulated sunlight illumination. This intermittent light exposure revealed transient photocurrent spikes attributed to hole accumulation at the electrode–electrolyte interface. Without co-catalyst loading, both bare Ta₃N₅ and MTN-X samples displayed relatively low photocurrent densities, limited by significant electron–hole recombination and stability issues under illumination. The recorded current densities at 1.23 V_{RHE} for Ta₃N₅, MTN-0.1, MTN-0.3, and MTN-0.5 were 0.78 mA cm⁻², 2 mA cm⁻², 1 mA cm⁻², and 0.8 mA cm⁻², respectively (Fig. 10(a)).

Notably, the $Co(OH)_x$ surface modification enhanced photocurrent densities for both bare and Mo-doped samples, as illustrated in Fig. 10(b). For bare Ta₃N₅ with co-catalyst, the photocurrent density reached 0.86 mA cm⁻² at 1.23 V_{RHE}, while MTN-0.1-Co achieved the highest photocurrent, peaking at 3.7 mA cm⁻² at the same potential, which is also higher than values reported in the previous literature.[12,58,64,65] This substantial increase in photocurrent density with Mo doping is attributed to improved light absorption, charge separation, charge transfer, and reaction kinetics. However, further increasing the Mo content beyond 0.1 M resulted in decreased current densities, likely due to scattering from impurities or defect formation from excess Mo. A detailed summary of the PEC results is provided in Tables 3 and 4.

The onset potentials, identified as the points at which the photocurrent density reached 0.2 mA cm⁻², are depicted in Fig. 10(c) and (d), with further details in Tables 3 and 4. For
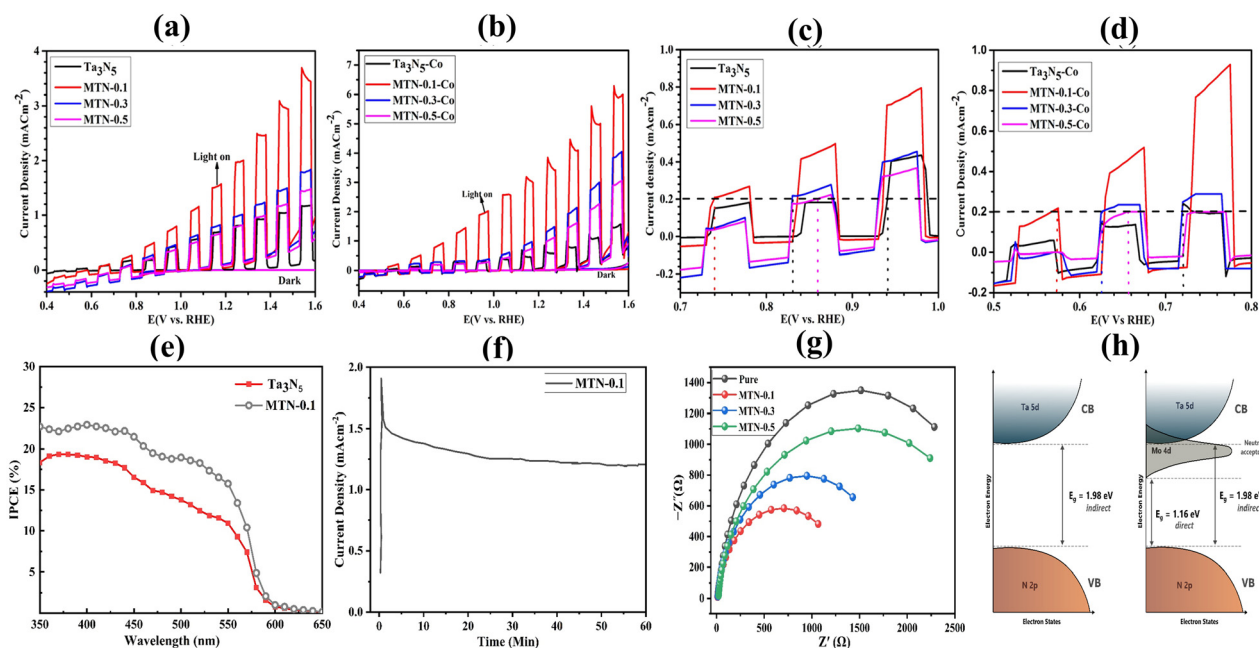
Fig. 10 LSV curves of pure Ta₃N₅ and MTN-X (a) without and (b) with the addition of co-catalyst under dark and chopped conditions. Representations of the onset potential of pure and Mo-doped Ta₃N₅ with (c) and without (d) co-catalyst. (e) IPCE at 1.23 V_{RHE}. (f) Time course photocurrent density curve of MTN-0.1 in 1 M KOH aqueous solution (pH 13.6) under AM 1.5G simulated sunlight illumination at 1.23 V_{RHE}. (g) Nyquist plots of Ta₃N₅, MTN-0.1, MTN-0.3 and MTN-0.5. (h) Energy level diagram of pure and Mo-doped Ta₃N₅.

Table 3 Water oxidation activity of bare Ta_3N_5 and MTN-X without co-catalyst

	Ta_3N_5	MTN-0.1	MTN-0.3	MTN-0.5
J at 1.23 V_{RHE} (mA cm^{-2})	0.78	2	1	0.8
J at 1.54 V_{RHE} (mA cm^2)	1.16	3	1.78	1.43
Onset potential (V_{RHE})	0.94	0.73	0.83	0.86

Table 4 Water oxidation activity of bare Ta_3N_5 and MTN-X with co-catalyst

	Ta_3N_5-Co	MTN-0.1-Co	MTN-0.3-Co	MTN-0.5-Co
J at 1.23 V_{RHE} (mA cm^{-2})	0.86	3.7	1.30	1
J at 1.54 V_{RHE} (mA cm^{-2})	1.56	6.1	3.8	2.9
Onset potential (V_{RHE})	0.72	0.57	0.62	0.66

bare Ta_3N_5, the onset potential was determined to be 0.94 V_{RHE} (Fig. 10(a)). Mo-doped samples, MTN-0.1, MTN-0.3, and MTN-0.5, exhibited onset potentials of 0.73 V_{RHE}, 0.83 V_{RHE}, and 0.86 V_{RHE}, respectively, indicating a cathodic shift due to Mo incorporation, effectively reducing the onset potentials compared to bare Ta_3N_5. This shift aligns with the photocurrent density results, where MTN-0.1 showed the highest current density. Following co-catalyst $(Co(OH)_x)$ (Fig. 10(d)) modification, MTN-0.1-Co demonstrated the lowest onset potential at 0.57 V_{RHE}, highlighting the enhanced PEC performance at this Mo concentration. These observations are consistent with the literature, which reports a similar cathodic shift in onset potential with Zr doping in Ta_3N_5. This study confirms that Mo doping in Ta_3N_5 is an effective strategy to optimize surface defects and minimize electron–hole recombination, enhancing photocatalytic activity.[22,26,64] After PEC tests, XRD and UV-Vis analyses were performed (Fig. S8 and S9†). These results match well with those of the counterparts (Fig. 6 and 7) showing that the materials do not exhibit any phase change.

The bulk charge separation and surface charge transfer efficiency were calculated based on established literature[23,65] as shown in Fig. S9.† Compared to pure Ta_3N_5, Mo doping significantly enhances both bulk and surface charge separation efficiencies (Fig. S9(a) and (b)†). The bulk charge separation efficiency at 1.23 V_{RHE} is 16.79% for pure Ta_3N_5, while for MTN-0.1 it is 31.63%. The surface charge transfer is improved by a factor of 3.55 as compared to the pure Ta_3N_5 sample.

To evaluate the photostability, tests were conducted for MTN-0.1 under AM 1.5G irradiation at 1.23 V_{RHE}, as shown in Fig. 10(f). The results demonstrate that MTN-0.1 retained 64% of its initial photocurrent after 60 min of continuous irradiation. Thus, further efforts are required to improve its stability.[20,23,65] To confirm the enhancement of PEC activity in Ta_3N_5 through Mo doping, the incident photon-to-current efficiency (IPCE) was measured as a function of photon wave-length at 1.23 V_{RHE}, as shown in Fig. 10(e). As one can observe, the pristine Ta_3N_5 electrode shows an IPCE of about 20%,[65] and after Mo doping it was increased to *ca.* 28%. Furthermore, these findings align well with the bulk charge separation efficiency and surface charge transfer efficiency, as presented in Fig. S11(a and b).†[23,58,64]

To investigate the interfacial charge transfer in pure and Mo-doped Ta_3N_5, electrochemical impedance spectroscopy (EIS) measurements were performed. The Nyquist plots and corresponding fitted results are shown in Fig. 10(g), confirming that the MTN-0.1 sample exhibits a significantly lower charge transfer resistance (1400 Ω) compared to that of pure Ta_3N_5 (3020 Ω), MTN-0.3 (1893 Ω), and MTN-0.5 (2958 Ω). These results clearly indicate that MTN-0.1 possesses superior interfacial charge transfer properties, contributing to its enhanced PEC performance.

6. Conclusion

In this study, we theoretically and experimentally demonstrated the doping of Mo into Ta_3N_5. Using GGA and GGA+U functionals, we systematically calculated the electronic and optical properties of bare and Mo-doped Ta_3N_5. The stability of Mo-doped Ta_3N_5 was confirmed through formation energy calculations. Importantly, the electronic band structure analysis indicates a transition from an indirect to a direct bandgap semiconductor upon Mo doping. The bandgap narrowing observed is attributed to unoccupied Mo 4d states contributing to the conduction band, as confirmed by PDOS analysis. Additionally, theoretical calculations reveal a redshift in the absorption spectrum toward lower energy, enhancing light absorption in the visible range. The strong optical anisotropy of both bare and Mo-doped Ta_3N_5 was corroborated by the calculated optical properties. An enhancement of the dielectric properties was observed, and the dielectric constant increased from 6.0 to 8.31 with Mo doping. The reflectivity at the optical bandgap decreased from 35% to 29%, while the static refractive index increased from 2.52 to 2.89. These results highlight the improved interaction of the material with electromagnetic radiation due to Mo doping. Mo-doped Ta_3N_5 photoanodes were experimentally prepared by hydrothermally introducing Mo dopants into Ta_2O_5 nanotubes, followed by a subsequent nitridation process. Comprehensive characterization using XPS, EDX, and Raman spectroscopy confirmed the successful incorporation of Mo into the Ta_3N_5 lattice. Structural, morphological, electrical, and optical analyses show that the Mo dopant replaces Ta lattice sites, introducing donor states below the conduction band. In line with the theoretical results, XPS has also shown that Mo doping suppresses the formation of reduced Ta species. Mo doping substantially enhanced the PEC performance of Ta_3N_5 photoanodes. When decorated with $Co(OH)_x$ as a co-catalyst, the 0.1 M Mo-doped Ta_3N_5 served as the best-performing photoanode, delivering a photocurrent density of 3.7 mA cm^{-2} at 1.23 V_{RHE}. This work provides a solid foundation for future research into tailored

doping strategies to optimize the performance of Ta_3N_5 based photoanodes for green energy applications.

Data availability

Conflicts of interest

The authors declare no conflict of interest.

Acknowledgements

References

1 D. Liu and Y. Kuang, Particle-Based Photoelectrodes for PEC Water Splitting: Concepts and Perspectives, *Adv. Mater.*, 2024, **19**, 1–30, DOI: **10.1002/adma.202311692**.

2 S. Khan, *et al.*, Revealing the true impact of interstitial and substitutional nitrogen doping in TiO2 on photoelectrochemical applications, *J. Mater. Chem. A*, 2021, **9**(20), 12214–12224, DOI: **10.1039/d0ta11494d**.

3 T. Zhou, *et al.*, Carbon quantum dots modified anatase/ rutile TiO2 photoanode with dramatically enhanced photoelectrochemical performance, *Appl. Catal., B*, 2020, **269**(800), 118776, DOI: **10.1016/j.apcatb.2020.118776**.

4 T. Zhou, *et al.*, Bird-nest structured ZnO/TiO2 as a direct Z-scheme photoanode with enhanced light harvesting and carriers kinetics for highly efficient and stable photoelectrochemical water splitting, *Appl. Catal., B*, 2020, **267**(800), 118599, DOI: **10.1016/j.apcatb.2020.118599**.

5 T. Zhou, *et al.*, Electrochemically reduced TiO2 photoanode coupled with oxygen vacancy-rich carbon quantum dots for synergistically improving photoelectrochemical performance, *Chem. Eng. J.*, 2021, **425**(800), 131770, DOI: **10.1016/j. cej.2021.131770**.

6 T. Zhou, *et al.*, Dramatically enhanced solar-driven water splitting of BiVO4 photoanode via strengthening hole transfer and light harvesting by co-modification of CQDs

and ultrathin β-FeOOH layers, *Chem. Eng. J.*, 2021, **403**(800), 126350, DOI: **10.1016/j.cej.2020.126350**.

7 T. Zhou, *et al.*, Oxygen vacancy-abundant carbon quantum dots as superfast hole transport channel for vastly improving surface charge transfer efficiency of BiVO4 photoanode, *Chem. Eng. J.*, 2022, **431**(P4), 133414, DOI: **10.1016/j.cej.2021.133414**.

8 T. Hisatomi, J. Kubota and K. Domen, *Recent advances in semiconductors for photocatalytic and photoelectrochemical water splitting*, Royal Society of Chemistry, 2014. DOI: **10.1039/c3cs60378d**.

9 F. E. Osterloh, Inorganic nanostructures for photoelectrochemical and photocatalytic water splitting, *Chem. Soc. Rev.*, 2013, **42**(6), 2294–2320, DOI: **10.1039/c2cs35266d**.

10 M. Inaba, K. Katayama and W. Y. Sohn, Cooperative effects of surface and interface treatments in a hematite (α-Fe2O3) photo-anode on its photo-electrochemical performance, *Sustainable Energy Fuels*, 2020, **4**(5), 2174–2183, DOI: **10.1039/c9se01081e**.

11 C. Wang, *et al.*, Synthesis of Nanostructured BaTaO2N Thin Films as Photoanodes for Solar Water Splitting, *J. Phys. Chem. C*, 2016, **120**(29), 15758–15764, DOI: **10.1021/acs. jpcc.5b11564**.

12 T. Higashi, *et al.*, Surface-modified ta3n5 photoanodes for sunlight-driven overall water splitting by photoelectrochemical cells, *Catalysts*, 2021, **11**(5), 1–15, DOI: **10.3390/ catal11050584**.

13 L. Cui, M. Wang and Y. X. Wang, Nitrogen vacancies and oxygen substitution of Ta3N5: First-principles investigation, *J. Phys. Soc. Jpn.*, 2014, **83**(11), 1–4, DOI: **10.7566/ JPSJ.83.114707**.

14 A. Dabirian and R. Van De Krol, Resonant optical absorption and defect control in Ta3N 5 photoanodes, *Appl. Phys. Lett.*, 2013, **102**(3), DOI: **10.1063/1.4788930**.

15 Y. Pihosh, *et al.*, Ta3N5-Nanorods enabling highly efficient water oxidation: Via advantageous light harvesting and charge collection, *Energy Environ. Sci.*, 2020, **13**(5), 1519–1530, DOI: **10.1039/d0ee00220h**.

16 T. Higashi, *et al.*, *Environmental Science anode for efficient and durable solar water splitting*, 2022, pp. 4761–4775, DOI: **10.1039/d2ee02090d**.

17 Y. Li, *et al.*, Cobalt phosphate-modified barium-doped tantalum nitride nanorod photoanode with 1.5% solar energy conversion efficiency, *Nat. Commun.*, 2013, **4**, 2566, DOI: **10.1038/ncomms3566**.

18 Y. Xie, Y. Wang, Z. Chen and X. Xu, Role of Oxygen Defects on the Photocatalytic Properties of Mg-Doped Mesoporous Ta3 N5, *ChemSusChem*, 2016, **9**(12), 1403–1412, DOI: **10.1002/cssc.201600193**.

19 J. Eichhorn, S. P. Lechner, C. M. Jiang, G. Folchi Heunecke, F. Munnik and I. D. Sharp, Indirect bandgap, optoelectronic properties, and photoelectrochemical characteristics of high-purity Ta3N5 photoelectrodes, *J. Mater. Chem. A*, 2021, **9**(36), 20653–20663, DOI: **10.1039/d1ta05282a**.

20 L. Pei, Z. Xu, Z. Shi, H. Zhu, S. Yan and Z. Zou, Mg-doped Ta3N5 nanorods coated with a conformal CoOOH layer for water oxidation: Bulk and surface dual modification of

photoanodes, *J. Mater. Chem. A*, 2017, **5**(38), 20439–20447, DOI: **10.1039/c7ta06227c**.

21 S. Grigorescu, *et al.*, Tungsten doping of Ta3N5-nanotubes for band gap narrowing and enhanced photoelectrochemical water splitting efficiency, *Electrochem. Commun.*, 2015, **51**, 85–88, DOI: **10.1016/j.elecom.2014.12.019**.

22 X. Zou, X. Han, C. Wang, Y. Zhao, C. Du and B. Shan, Carrier engineering of Zr-doped Ta3N5 film as an efficient photoanode for solar water splitting, *Sustainable Energy Fuels*, 2021, **5**(11), 2877–2883, DOI: **10.1039/d1se00640a**.

23 J. Feng, *et al.*, Ge-mediated modification in Ta3N5 photoelectrodes with enhanced charge transport for solar water splitting, *Chem. – Eur. J.*, 2014, **20**(49), 16384–16390, DOI: **10.1002/chem.201402760**.

24 Y. Kado, *et al.*, Enhanced water splitting activity of M-doped Ta3N5 (M = Na, K, Rb, Cs), *Chem. Commun.*, 2012, **48**(69), 8685–8687, DOI: **10.1039/c2cc33822j**.

25 J. Xiao, *et al.*, Simultaneously tuning the defects and surface properties of Ta3N5 nanoparticles by Mg–Zr codoping for significantly accelerated photocatalytic H2 evolution, *J. Am. Chem. Soc.*, 2021, **143**, 10059–10064, DOI: **10.1021/jacs.1c04861**.

26 L. I. Wagner, *et al.*, Defect Engineering of Ta3N5 Photoanodes: Enhancing Charge Transport and Photoconversion Efficiencies via Ti Doping, *Adv. Funct. Mater.*, 2023, 2306539, DOI: **10.1002/adfm.202306539**.

27 M. Rohloff, *et al.*, Mo-doped BiVO4 thin films-high photoelectrochemical water splitting performance achieved by a tailored structure and morphology, *Sustainable Energy Fuels*, 2017, **1**(8), 1830–1846, DOI: **10.1039/c7se00301c**.

28 E. Engel and S.H. Vosko, Exact exchange-only potentials and the virial relation as microscopic criteria for generalized gradient approximations, *Phys. Rev. B*, 1993, **47**(20), 13164–13174, DOI: **10.1103/PhysRevB.47.13164**.

29 J. Kozlowski, D. Perchak and K. Burke, Generalized Gradient Approximation Made Thermal, 2023, [Online]. Available: **https://arxiv.org/abs/2308.03319**.

30 S. A. Tolba, K. M. Gameel, B. A. Ali, H. A. Almossalami and N. K. Allam, The DFT+U: Approaches, Accuracy, and Applications, in *Density Functional Calculations - Recent Progresses of Theory and Application*, InTech, 2018. DOI: **10.5772/intechopen.72020**.

31 H. Jouypazadeh, H. Farrokhpour and M. M. Momeni, A DFT study of the water-splitting photocatalytic properties of pristine, Nb-doped, and V-doped Ta3N5 monolayer nanosheets, *Surf. Interfaces*, 2021, **26**, 101379, DOI: **10.1016/j.surfin.2021.101379**.

32 J. Wang, *et al.*, Charge compensation doping to improve the photocatalytic and photoelectrochemical activities of Ta3N5: A theoretical study, *Appl. Catal., B*, 2019, **244**, 502–510, DOI: **10.1016/j.apcatb.2018.11.076**.

33 A. Janotti, J. B. Varley, P. Rinke, N. Umezawa, G. Kresse and C. G. Van De Walle, Hybrid functional studies of the oxygen vacancy in TiO2, *Phys. Rev. B:Condens. Matter Mater. Phys.*, 2010, **81**(8), DOI: **10.1103/PhysRevB.81.085212**.

34 P. Krisna Das, *et al.*, Nanoporous Ta3N5: Via electrochemical anodization followed by nitridation for solar

water oxidation, *Dalton Trans.*, 2020, **49**(42), 15023–15033, DOI: **10.1039/d0dt03056b**.

35 J. Wang, T. Fang, L. Zhang, J. Feng, Z. Li and Z. Zou, Effects of oxygen doping on optical band gap and band edge positions of Ta3N5 photocatalyst: A GGA + U calculation, *J. Catal.*, 2014, **309**, 291–299, DOI: **10.1016/j.jcat.2013.10.014**.

36 M. Cococcioni and S. D. Gironcoli, Linear response approach to the calculation of the effective interaction parameters in the LDA+U method, *Phys. Rev. B:Condens. Matter Mater. Phys.*, 2005, **71**(3), 035105, DOI: **10.1103/PhysRevB.71.035105**.

37 V. N. Jafarova and G. S. Orudzhev, Structural and electronic properties of ZnO: A first-principles density-functional theory study within LDA(GGA) and LDA(GGA)+U methods, *Solid State Commun.*, 2021, **325**, 114166, DOI: **10.1016/j.ssc.2020.114166**.

38 R. Tesch and P. M. Kowalski, Hubbard U parameters for transition metals from first principles, *Phys. Rev. B*, 2022, **105**(19), DOI: **10.1103/PhysRevB.105.195153**.

39 P. Rauch, F. J. Disalvo, Y. Wu and G. Ceder, First principles study on Ta3N5:Ti3O3N2 solid solution as a water-splitting photocatalyst, *Cryst. Struct. Commun.*, 1991, **305**(1972), 66–69, DOI: **10.1107/S0108270191005231**.

40 H. Jouypazadeh, H. Farrokhpour and M. M. Momeni, Theoretical investigation of the water splitting photocatalytic properties of pristine, Nb and V doped, and Nb-V co-doped (1 1 1) TaON nanosheets, *Appl. Surf. Sci.*, 2021, **541**, 148572, DOI: **10.1016/j.apsusc.2020.148572**.

41 M. Harb, *et al.*, Tuning the properties of visible-light-responsive tantalum (oxy)nitride photocatalysts by non-stoichiometric compositions: A first-principles viewpoint, *Phys. Chem. Chem. Phys.*, 2014, **16**(38), 20548–20560, DOI: **10.1039/c4cp03594a**.

42 W. J. Chun, *et al.*, Conduction and valence band positions of Ta2O5, TaOn, and Ta3N5 by UPS and electrochemical methods, *J. Phys. Chem. B*, 2003, **107**(8), 1798–1803, DOI: **10.1021/jp027593f**.

43 J. Wang, T. Fang, L. Zhang, J. Feng, Z. Li and Z. Zou, Effects of oxygen doping on optical band gap and band edge positions of Ta 3 N 5 photocatalyst : A GGA + U calculation, *J. Catal.*, 2014, **309**, 291–299, DOI: **10.1016/j.jcat.2013.10.014**.

44 C. M. Fang, *et al.*, The electronic structure of tantalum (oxy)nitrides TaON and Ta3N5, *J. Mater. Chem.*, 2001, **11**(4), 1248–1252, DOI: **10.1039/b005751g**.

45 F. Kong and G. Jiang, Nonlinear optical response of wurtzite ZnO from first principles, *Physica B: Condens. Matter*, 2009, **404**(16), 2340–2344, DOI: **10.1016/j.physb.2009.04.041**.

46 J. Wang, A. Ma, Z. Li, J. Jiang, J. Feng and Z. Zou, Unraveling the mechanism of 720 nm sub-band-gap optical absorption of a Ta3N5 semiconductor photocatalyst: A hybrid-DFT calculation, *Phys. Chem. Chem. Phys.*, 2015, **17**(12), 8166–8171, DOI: **10.1039/c4cp04931d**.

47 H. Yin, *et al.*, Shallow Oxygen Substitution Defect to Deeper Defect Transformation Mechanism in Ta3N5under Light

Irradiation, *J. Phys. Chem. Lett.*, 2021, **12**(15), 3698–3704, DOI: **10.1021/acs.jpclett.1c00767**.

48　R. Khan, K. Ur Rahman, Q. Zhang, A. U. Rahman, S. Azam and A. Dahshan, The effect of substitutional doping of Yb2+ on structural, electronic, and optical properties of CsCaX 3(X: Cl, Br, I) phosphors: A first-principles study, *J. Phys.: Condens. Matter*, 2022, **34**(6), DOI: **10.1088/1361-648X/ac3583**.

49　A. H. Reshak, Electronic structure and dispersion of optical function of tantalum nitride as a visible light photo-catalyst, *Comput. Mater. Sci.*, 2014, **89**, 45–51, DOI: **10.1016/j.commatsci.2014.03.035**.

50　S. Khan, *et al.*, Structural, optical and photoelectrochemical characterizations of monoclinic Ta3N5 thin films, *Phys. Chem. Chem. Phys.*, 2015, **17**(37), 23952–23962, DOI: **10.1039/c5cp03645c**.

51　T. Wen, *et al.*, Growth behavior of tantalum oxide nanotubes during constant current anodization, *Electrochem. Commun.*, 2021, **128**, 107073, DOI: **10.1016/j.elecom.2021.107073**.

52　T. Fang, *et al.*, Exploring facile strategies for high-oxidation-state metal nitride synthesis: carbonate-assisted one-step synthesis of Ta3N5 films for solar water splitting, *Sci. Bull.*, 2018, **63**(21), 1404–1410, DOI: **10.1016/j.scib.2018.10.005**.

53　S. Khan, S. R. Teixeira and M. J. L. Santos, Controlled thermal nitridation resulting in improved structural and photoelectrochemical properties from Ta3N5 nanotubular photoanodes, *RSC Adv.*, 2015, **5**(125), 103284–103291, DOI: **10.1039/c5ra17227f**.

54　S. Khan, M. J. L. Santos, C. F. Malfatti, J. Dupont and S. R. Teixeira, Pristine Ta_3N_5 Nanotubes: Trap-Driven High External Biasing Perspective in Semiconductor/Electrolyte Interfaces, *Chem. – Eur. J.*, 2016, **22**(51), 18269–18627, DOI: **10.1002/chem.201603246**.

55　G. Fan, X. Wang, H. Fu, J. Feng, Z. Li and Z. Zou, Compensation of band-edge positions in titanium-doped Ta3 N5 photoanode for enhanced water splitting performance: A first-principles insight, *Phys. Rev. Mater.*, 2017, **1**(3), DOI: **10.1103/PhysRevMaterials.1.035403**.

56　S. Khan, *et al.*, Effect of Oxygen Content on the Photoelectrochemical Activity of Crystallographically Preferred Oriented Porous Ta3N5 Nanotubes, *J. Phys. Chem. C*, 2015, **119**(34), 19906–19914, DOI: **10.1021/acs.jpcc.5b05475**.

57　J. Eichhorn, S. P. Lechner, C. M. Jiang, G. Folchi Heunecke, F. Munnik and I. D. Sharp, Indirect bandgap, optoelectronic properties, and photoelectrochemical characteristics of high-purity Ta3N5photoelectrodes, *J. Mater. Chem. A*, 2021, **9**(36), 20653–20663, DOI: **10.1039/d1ta05282a**.

58　C. Shao, R. Chen, Y. Zhao, Z. Li, X. Zong and C. Li, Reducing the surface defects of Ta3N5photoanode towards enhanced photoelectrochemical water oxidation, *J. Mater. Chem. A*, 2020, **8**(44), 23274–23283, DOI: **10.1039/d0ta08121c**.

59　E. Nurlaela, M. Harb, S. Del Gobbo, M. Vashishta and K. Takanabe, Combined experimental and theoretical assessments of the lattice dynamics and optoelectronics of TaON and Ta3N5, *J. Solid State Chem.*, 2015, **229**, 219–227, DOI: **10.1016/j.jssc.2015.06.029**.

60　H. Hajibabaei, O. Zandi and T. W. Hamann, Tantalum nitride films integrated with transparent conductive oxide substrates: Via atomic layer deposition for photoelectrochemical water splitting, *Chem. Sci.*, 2016, **7**(11), 6760–6767, DOI: **10.1039/c6sc02116f**.

61　Y. W. Kim, *et al.*, Surface-Modified Ta3N5 Nanocrystals with Boron for Enhanced Visible-Light-Driven Photoelectrochemical Water Splitting, *ACS Appl. Mater. Interfaces*, 2017, **9**(42), 36715–36722, DOI: **10.1021/acsami.7b09040**.

62　W. J. Chun, *et al.*, Conduction and valence band positions of Ta2O5, TaOn, and Ta3N5 by UPS and electrochemical methods, *J. Phys. Chem. B*, 2003, **107**(8), 1798–1803, DOI: **10.1021/jp027593f**.

63　Y. He, *et al.*, What Limits the Performance of Ta3N5 for Solar Water Splitting?, *Chem*, 2016, **1**(4), 640–655, DOI: **10.1016/j.chempr.2016.09.006**.

64　C. Dong, X. Zhang, Y. Ding, Y. Zhang and Y. Bi, Unveiling the high activity origin of NiFe catalysts decorated Ta3N5 photoanodes for oxygen evolution reaction, *Appl. Catal., B*, 2023, **338**, 123055, DOI: **10.1016/j.apcatb.2023.123055**.

65　Z. Wang, *et al.*, Insight into the charge transfer in particulate Ta3N5 photoanode with high photoelectrochemical performance, *Chem. Sci.*, 2016, **7**(7), 4391–4399, DOI: **10.1039/c6sc00245e**.